CORA Cork Open Research Archive
Cartlann Taighde Oscailte Chorcaí

Title	Enhanced oxidation activity from modified ceria: MnOx-ceria, CrOx-ceria and Mg doped VOx-ceria
Authors	Nolan, Michael;Ganduglia-Pirovano, M. Verónica
Publication date	2016-03-09
Original Citation	NOLAN, M. and GANDUGLIA-PIROVANO, M. V. (2016) 'Enhanced oxidation activity from modified ceria: MnOx–ceria, CrOx–ceria and Mg doped VOx–ceria', Applied Catalysis B: Environmental, 197, pp. 313-323. doi:10.1016/j.apcatb.2016.03.015
Type of publication	Article (peer-reviewed)
Link to publisher's version	10.1016/j.apcatb.2016.03.015
Rights	© 2016, Elsevier B.V. All rights reserved. This manuscript version is made available under the CC-BY-NC-ND 4.0 license http://creativecommons.org/licenses/by-nc-nd/4.0/ - http://creativecommons.org/licenses/by-nc-nd/4.0/
Download date	2026-10-31 05:07:49
Item downloaded from	https://hdl.handle.net/10468/3265

UCC
University College Cork, Ireland
Coláiste na hOllscoile Corcaigh

*Revised Manuscript
Click here to view linked References

Enhanced Oxidation Activity from Modified Ceria: MnO_x-ceria, CrO_x-ceria and Mg doped VO_x-ceria

Michael Nolan

Tyndall National Institute, University College Cork, Lee Maltings, Cork, Ireland

M. Verónica Ganduglia-Pirovano

Instituto de Catálisis y Petroleoquímica of the Consejo Superior de Investigaciones Científicas, Madrid, Spain

Abstract

Ceria is an important component of catalysts for oxidation reactions that proceed through the Mars-van Krevelen mechanism, promoting activity. A paradigm example of this is the VO_x-CeO_2 system for oxidative dehydrogenation reactions, where vanadium oxide species are supported on ceria and a special synergy between them is behind the enhanced activity: reduction of the catalyst is promoted by ceria undergoing reduction. This leads to favourable oxygen vacancy formation and hydrogen adsorption energies –useful descriptors for the oxidation activity of VO_x-CeO_2 catalysts. In this paper, we examine if this promoting effect on ceria-based catalysts holds for other metal oxide modifiers and we investigate MnO_n- and CrO_n-CeO_2(111) (n=0–4) as examples. We show, combining density functional theory calculations and statistical

thermodynamics that similarly to the vanadia modifier, the stable species in each case is MnO_2- and CrO_2-CeO_2. Both show favourable energetics for oxygen vacancy formation and hydrogen adsorption, indicating that VO_2-CeO_2 is not the only system of this type that can have an enhanced activity for oxidation reactions. However, the mechanism involved in each case is different: CrO_2-CeO_2 shows similar properties to VO_2-CeO_2 with ceria reduction upon oxygen removal stabilising the 5+ oxidation state of Cr. In contrast, with MnO_2-CeO_2, Mn is preferentially reduced. Finally, a model system of VO_2-Mg:CeO_2 is explored that shows a synergy between VO_2 modification and Mg doping. These results shed light on the factors involved in active oxidation catalysts based on supported metal oxides on ceria that should be taken into consideration in a rational design of such catalysts.

Introduction

Ceria-supported transition metal oxide catalysts are active for oxidation reactions that proceed through the so-called Mars-van Krevelen or redox-type mechanism [1]. Depositing vanadia on ceria leads to a particularly active catalytic system [2, 3]. This activity arises from the ability of ceria to easily accommodate electrons in localized Ce-4f orbitals. Ceria is directly involved in the redox process, as two electrons are accommodated in Ce f states forming two Ce^{3+} ions whereas vanadium remains fully oxidized (V^{5+}) [4, 5]. The question arises on the uniqueness of vanadia modifier leading to enhance activity and the possibility to rationally design improved ceria-supported transition metal oxide catalysts for oxidation reactions.

To investigate if VO_x-modified ceria is unique in showing a synergy between the ceria and oxide modifier and if one can conceive of substituting for vanadium oxide another transition metal oxide to give similar, or better, activity for oxidative reactions, we have undertaken an examination of other possible transition metal oxide modifiers of ceria (111). We explore Mn and Cr as transition metals that could be alternatives to V, while being economical in cost and abundant. This approach allows us to widen our understanding of MO_x-modified ceria oxidation catalysts, giving useful insights for the design of these catalysts. To this end, we present in this paper a periodic density functional theory (DFT+*U*) study (incorporating the Hubbard +U correction [6, 7]) of the ceria (111) surface modified with MnO_n and CrO_n species (n=0–4), which similar to vanadium can take multiple oxidation states, and we investigate two key aspects of these systems: (1) The stability of different compositions of MnO_n and CrO_n-modified CeO_2(111) and the resulting transition metal and Ce oxidation states, (2) The formation energy of oxygen vacancies and adsorption of hydrogen as descriptors of the oxidative power of these composite systems.

Moreover, to improve the oxidative power of ceria and of other oxides, such as TiO_2 or La_2O_3, substitutional cation doping of a foreign metal at a host cation site has been studied, using both modelling [8 - 18] and experiment [19 - 24] and combined modelling and experimental studies, e.g. [19, 20]; the joint modelling and experimental papers are of particular interest as these indicate the promoting effect of the dopant on reducibility of the host oxides. Relying on energies of oxygen vacancy formation as descriptors for Mars-van Krevelen type reactions, in general, substitutional doping of ceria with metal dopants tends to enhance the oxidative power of metal oxides by reducing the cost of oxygen vacancy formation compared to undoped ceria [8 - 24]. This makes removal of oxygen from the oxide more favourable and should enhance its activity, e.g in Ref [13, 14] where Krcha et al discuss trends in methane activation on doped ceria. The origins of this enhanced activity arise from a number of factors: dopant ionic radius and coordination, distortions to the local atomic structure around the dopant that weaken the metal-oxygen bonds and relaxations after oxygen removal.

In a final contribution, we examine a model system that combines VO_2 modification of $CeO_2(111)$ with substitutional cation doping in ceria, by studying Mg-doped $CeO_2(111)$, modified with VO_2 (VO_2-Mg:CeO_2), to investigate if there is a synergy between doping and surface modification in enhancing the oxidative ability of ceria.

Throughout this paper we follow Popa et al [25] and use MO_x (M = V, Cr, Mn) if we refer to ceria modified with M-oxide in general or from experiment and MO_n (n = 0–4) if we refer to the particular model system MO_n-CeO_2 that is studied with DFT. To investigate stability, we follow ref [25] to determine the stability of different MO_n compositions on ceria (111) allowing us to identify which are the most stable systems under given conditions. To investigate the oxidative power of MO_x-CeO_2, we compute the cost to form an oxygen vacancy (relative to ½ gas phase

O_2) and the adsorption energy of a hydrogen atom (relative to ½ gas phase H_2) at MO_x-CeO_2. The former relates to the reaction energy as a water molecule desorbs and an oxygen vacancy is formed in the catalyst after the oxidation cycle [4, 26, 27], and the latter relates to the rate-limiting step in oxidative dehydrogenation (ODH) reactions, namely the first hydrogen abstraction [4, 28].

Finally, it is known experimentally that the vanadia catalyst exhibits only high activity when present as submonolayer or monolayer species on the support [1, 29, 30]. Recent theoretical work has shown that aggregates of VO_n-CeO_2 are more stable than isolated monomers [31], but the kinetic barrier for their diffusion to form the aggregates is sufficiently high [32], suggesting that studying the monomeric MO_x-CeO_2 system, as in refs [4, 5, 25] is reasonable.

We find that at 1 atm and at 400 K, typical of previous work on VO_x-modified ceria [25], MnO_x-CeO_2 is most stable as MnO_2-CeO_2(111) and CrO_x-CeO_2 is most stable as CrO_2-CeO_2(111), with Mn taking a 4+ oxidation state and Cr a 5+ oxidation state. Ceria therefore stabilizes a high oxidation state of both metals. Although for Cr, this result appears similar to V in VO_2-CeO_2(111), we must remember that for Cr (and Mn) higher oxidation states can be attained. MnO_2-CeO_2 and CrO_2-CeO_2 are more reactive towards oxygen vacancy formation and hydrogenation than bare CeO_2, indicating that they are an interesting alternative to VO_x-CeO_2. Reduction of MnO_2-CeO_2 is different to VO_2-CeO_2 with Mn reduction preferred over Ce reduction. Finally, the combination of Mg doping and VO_2 modification is predicted to result in enhanced oxidation activity compared to doping or VO_2 modification alone. The results of this work therefore expand the possibilities of well-understood ceria modifications for enhanced oxidation activity.

Methods

Periodic density functional theory (DFT) calculations were carried out within a plane wave basis set and periodic surface models of CeO_2(111) within the VASP 5.2 program package [33, 34]. A Hubbard *U* correction was added to the PBE exchange-correlation functional [35], giving the PBE+*U* method, that has been widely used for modelling ceria [4, 5, 25, 36, 37, 38, 39, 40, 41, 42, 43, 44, 45, 46, 47, 48, 49, 50]. The inadequacy of GGA functionals, such as PW91 or PBE to provide a proper account of the change in Ce oxidation state upon reduction has been well confirmed [40, 49, 50, 51]. The unphysical electron self-interaction in GGA functionals results in a complete failure of pure DFT in treating the electronic structure of reduced ceria in which the electrons left in the system upon neutral oxygen vacancy formation predominantly localize in atomic-like orbitals.

The value of the *U* parameters was set to be 4.5 eV on the Ce 4f states [37], a standard value of *U* in the literature on ceria bulk and surfaces and also used successfully to describe VO_n-modified CeO_2(111) [4, 5, 25, 31, 32, 36, 37, 39, 40]; we also tested that the overall results are insensitive to using an alternative value of U = 5 eV, as suggested in other studies [8, 40, 41, 42, 44, 51, 52]. These values are within the range 4.5 – 6.0 eV reported to provide localization of the excess charge [4, 5, 8, 25, 31, 32, 36, 37, 38, 39, 41, 42, 43, 44, 45, 46, 47, 48, 49, 50, 51, 52].

Many studies have applied the (periodic) DFT+*U* methodology to oxygen defects at CeO_2 surfaces, under a range of different scenarios (undoped, modified with dopants, modified with metals, modified with VO_n species), e.g. refs. [4, 5, 8, 25, 31, 32, 36, 37, 38, 39, 41, 42, 43, 44, 45, 46, 47, 48, 49, 50, 51, 52]. While there have been fewer hybrid DFT studies [9, 36, 38, 52, 53, 54], there is a clear consistency between the description of CeO_2 from the DFT+*U* set-up described above and that of hybrid DFT, in that all of these calculations satisfactorily described

(1) the localization of two electrons per O vacancy, that drives the $Ce^{4+} \rightarrow Ce^{3+}$ reduction, (2) the appearance of defect states lying inside the O2p–Ce5d ceria band gap, which too small values of *U* will not recover and (3) the qualitative trends in vacancy formation [4, 5, 8, 25, 31, 32, 36, 37, 38, 39, 41, 42, 43, 44, 45, 46, 47, 48, 49, 50, 51, 52], effect of doping [8, 53, 54] and surface modifications [25, 31, 32]. In these respects, the results of this extensive range of DFT+*U* studies are entirely consistent, despite the different DFT+*U* implementations.

However, care has to be taken in using DFT+*U* for calculations on transition metal and rare-earth oxide-based systems [55].*U* parameters can be derived from fitting structural and energetic parameters to experimental data or calculated by linear response theory [56]. It is important to mention that no single *U* parameter can describe all material properties with the same degree of accuracy [57]. For example, the difficult case of CO adsorption on CeO_2 (110) in ref [58, 59], shows that *U* = 4.5 or 5 eV results in CO overbinding compared to experiment. With *U* = 2 eV, the adsorption energy is consistent with experiment, but this comes at the cost of not describing the electronic structure of the ceria surface accurately. There are also questions regarding the specification of the atomic-like orbitals in DFT+*U* [40], the existence of multiple self-consistent solutions [60, 61, 62] to the electronic structure and the derivation of the "best" value for the *U* parameter which are still of great interest and debate. Finally, for the case of magnetic systems, the choice of the *U* value may also affect the energetic ordering of the possible magnetic solutions [63]. This is not a problem for reduced ceria as mentioned here below. Despite all of these non-fully satisfactory issues related to the DFT+*U* method, the present DFT+*U* set-up has proven to be robust in describing many trends for ceria-based systems in comparison to hybrid DFT and to experiment.

There may also be the question of a suitable DFT+*U* set-up for doped/modified ceria versus undoped/unmodified ceria. Firstly, the studies on doped ceria in the literature [8 -15, 20] continue to use the DFT+*U* set-up used in this paper, where *U* is sufficient to localise electrons on Ce sites, and there have been some comparisons made with hybrid DFT results where this DFT+*U* set-up is entirely consistent. Moreover, the DFT+*U* set-up used herein has been applied extensively to, for example, different compositions and structures of the VOx/ceria system, demonstrating clearly that it provides reliable results. This includes successfully describing $CeVO_4$, with Ce^{3+} and V^{5+} oxidation states, [64] and VO_n monomers and oligomers on ceria [25, 31]. In these latter studies, comparisons with the hybrid DFT HSE06 approach gave similar results for the key trends examined. In older studies, dopants in CeO_2 were studied with DFT+*U* and HSE06 [9, 53, 54] and the formation of localised Ce^{3+} was found with both approaches, demonstrating the consistency of the DFT+*U* set-up.

For other transition metal based materials systems, DFT+*U* has been widely used. Examples here include Cr deposition and oxidation on rutile TiO_2 (110) films [65], Mn-doping of CeO_2 [13, 14], Fe/FeOx based molecules [66], FeOx nanoclusters [67], transition metal olivines [68] and the formation of reduced Ti in TiO_2 bulk, surfaces and interfaces [69, 70, 71, 72]. Thus, in this work for Mn and Cr, which can take oxidation states with partially filled 3 d electronic states, we also apply the DFT+*U* correction to their 3d states. *U* values of 4.5 eV for Mn, typical of the range of values used for Mn 3d, e.g. refs. [13, 14, 73, 74], and 3.5 eV for Cr were used [65]. For V 3d states, no *U* parameter was used. This PBE+*U* set-up has been found to give a description of VO_n-CeO_2 that is comparable with the more expensive hybrid DFT HSE06 set-up [25, 31]

To describe the core-valence interaction, the PAW potentials [75] were used: specifically, the 12 valence electron Ce_h potential supplied with VASP5, the 6 valance electron oxygen potential,

the 6, 13 and 7 valence electron Cr, V and Mn potentials and a standard hydrogen potential. Spin polarised calculations are performed throughout this study. We assume a ferromagnetic arrangement of cerium spins (Ce^{3+}, $4f^1$) in all structures as the energy difference between the antiferromagnetic open-shell singlet and the ferromagnetic high-spin solutions is known to be small, e.g. not larger than 0.01 eV refs [36, 39]. In ref [25] on VO_n-CeO_2, a high spin configuration for the Ce spins was used throughout as the maximum differences in the total energy for different spin configurations were at most 0.05 eV, which is significantly smaller than the energy differences of interest, namely those between vacancy formation and H adsorption energies. For the modifiers, i.e. MnO_n- and CrO_n-, we have also examined the different spin states and we find that the highest spin state is the more stable. Hence, all results in the present study focus on high-spin states.

The cut-off energy is 500 eV, smearing uses the Methfessel-Paxton approach with sigma = 0.05 eV. k-point sampling is performed using a ($3 \times 3 \times 1$) Monkhorst-Pack grid, the quasi-Newton relaxation algorithm is used for the geometry relaxations, with convergence achieved when energy differences are smaller than 10^{-3} eV and forces are smaller than 0.02 eV/Å.

The ceria (111) surface slab is non-polar with 9 atomic layers (3 neutral O-Ce-O trilayers) in a (2×2) surface supercell expansion (testing of a larger (3×3) surface supercell gives no change to the results) and the bottom trilayer is fixed, while all other atoms are allowed to relax in a fixed supercell with no symmetry constraints.

We modifiy the ceria (111) surface with MnOn and CrOn, where $n = 0 - 4$ and calculate the stability over a wide temperature range at 1 atm pressure, using the approach previously described in ref [25]. The thermodynamic formalism used is described in detail and applied in

several studies. In brief, the (formal) formation of a manganese or chromium oxide species on the ceria surface from metal M (M = Mn, Cr) and oxygen is:

$$(CeO_2)_{12} + M + \frac{n}{2}O_2 \Leftrightarrow MO_n \bullet (CeO_2)_{12}$$

Where $(CeO_2)_{12}$ denotes the stoichiometry of the surface supercell of $CeO_2(111)$. This reaction has the following change in surface free energy

$$\Delta\gamma(T, p) = \frac{1}{A}[G[MO_n \bullet (CeO_2)_{12}] - G[(CeO_2)_{12}] - \mu[M] - \frac{n}{2}\mu[O_2](T, p)] \qquad (1)$$

Where $G[MO_n \bullet (CeO_2)_{12}]$ and $G[(CeO_2)_{12}]$ are the Gibbs free energies of the supercells used to model MO_n-$CeO_2(111)$ and the $CeO_2(111)$ surface at the indicated stoichiometries. $\mu[M]$ and $\mu[O_2]$ are the chemical potentials of the solid metal, M, and oxygen. A is the surface area.

If we insert the following

$$\Delta\mu[O](T, p)] = \frac{1}{2}[\mu[O_2](T, p) - E(O_2)] \qquad (2)$$

Into Eq. (1) above, we obtain

$$\Delta\gamma(T, p) = \frac{1}{A}[G[MO_n \bullet (CeO_2)_{12}] - G[(CeO_2)_{12}] - \mu[M] - \frac{n}{2}E[O_2] - n\Delta\mu[O](T, p)] \qquad (3)$$

The chemical potential of oxygen is related to the pressure and temperature conditions by assuming that the CeO_2 surface is in thermodynamic equilibrium with the gas phase. Since the O_2 atmosphere forms an ideal gas reservoir, the pressure dependence of $\Delta\mu[O](T, p)$ at a given temperature is given by ($\Delta\mu[O_2](0K) = E[O_2]$ and p^0 is the pressure of a reference state, p = 1 atm).

$$\Delta\mu[O](T,p)] = \frac{1}{2}[H(T,p^0) - H(0K,p^0) - TS(T,p^0) + RT\ \ln(p/p^0)] \quad (4)$$

In Eq. (4), the enthalpy, *H*, and entropy, *S*, at the temperature, *T*, can be taken from tabulated values (76). μ[M] is set equal to the DFT total energy of the metallic bulk Mn and Cr (E_{bulk}[Mn] and E_{bulk}[Cr], respectively).

The Gibbs free energies of the solid components in Eq. (3) are equated to the total energies from DFT that are calculated in our fixed volume supercells and at T = 0 K, so that:

$$\Delta\gamma(T,p) = \frac{1}{A}[E[MO_n \bullet (CeO_2)_{12}] - E[(CeO_2)_{12}] - E_{bulk}[M] - \frac{n}{2}E[O_2] - n\Delta\mu[O](T,p)] \quad (5)$$

The vibrational contributions and *pV* terms are neglected in this analysis. It has been previously shown that the vibrational contributions to the entropy tend to cancel out, and the influence of the *pV* term is even smaller [77, 78].

For a given chemical potential, we can then predict which $MO_n \bullet (CeO_2)_{12}$ surface structure is the most stable by searching for the surface model with the lowest surface free energy.

To examine the synergy between doping and VO_2 modification, we modify the Mg-doped CeO_2(111) surface with a compensating oxygen vacancy [20] with VO_2. To investigate the reactivity, oxygen atoms are removed from the MnOn and CrOn moiety and from the surface and the structures are relaxed. The oxygen vacancy formation and hydrogen adsorption energies are calculated (using MnO_2 as an example):

$E^{vac} = \{E(MnO\text{-}CeO_2) + 1/2E(O_2)\} - E(MnO_2\text{-}CeO_2)$ O vacancy formation

$E^{ads} = E(H\text{-}MnO_2\text{-}CeO_2) - \{E(MnO_2\text{-}CeO_2) + 1/2E\ (H_2)\}$ H adsorption

Key quantities of interest for this work are the oxidation states of Ce, Mn and Cr in the different compositions of MnO_n and CrO_n and after formation of oxygen vacancies and hydrogen adsorption. The occupation of the Mn and Cr 3d and Ce 4f states is obtained by integration of the site- and angular momentum-projected spin-resolved density of states and computing the spin magnetisations over spheres with radii chosen as the Wigner−Seitz radii of the corresponding PAW potentials. We also compute the net Bader charges (number of valence electron minus the computed Bader charge) of Cr, Mn and Cr in all calculations and together these quantities allow an assignment of the oxidation states of the cations in all structures.

3. Results

3.1. Modification of CeO_2(111) with MnO_n Species

For modification of CeO_2(111) with manganese oxide, and analogous to previous work on VO_n modified ceria, we consider the series Mn, MnO, MnO_2, MnO_3 and MnO_4; this is also followed for CrO_2-CeO_2. Figure 1 shows the stability plot for different MnO_n species on the CeO_2(111) surface at 1 atm pressure, allowing us to determine the most stable surface modifier under given conditions and the most stable structures for each composition are shown in figure 2. Following from the results in refs. [31, 32] which studied the aggregation of VO_n monomers to larger structures on CeO_2(111), we assume that the barrier for aggregation of MnO_n and CrO_n monomers is large so that it suffices to study monomeric species.

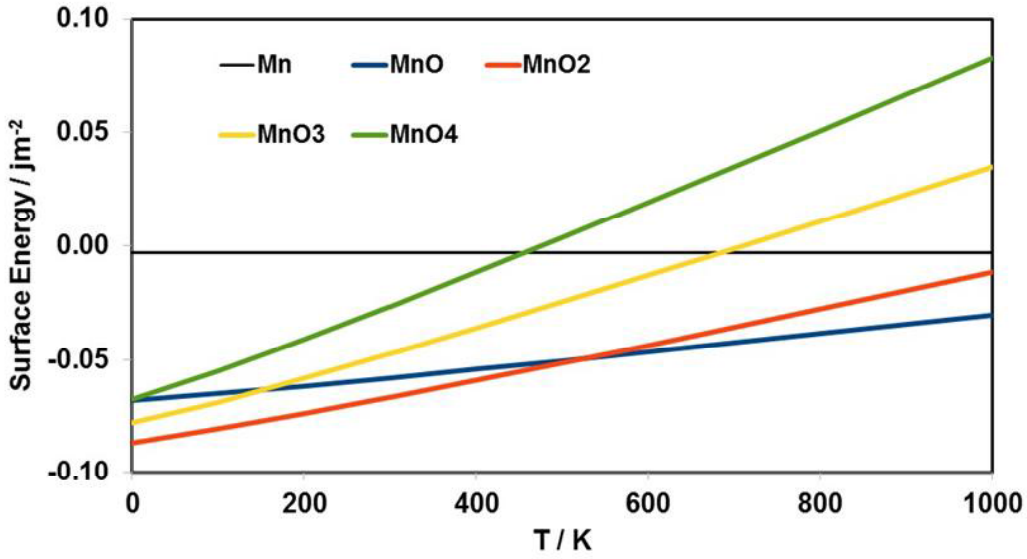


Figure 1: Plot of the surface energy of the MnO_n-CeO_2 system as a function of temperature at 1 atm.

At 1 atm pressure and at temperatures up to 575 K, the MnO_2 modifier is the most stable. Beyond this temperature, the MnO-CeO_2(111) structure is the most stable. Thus, under conditions typical for reactions such as ODH, the modification of the CeO_2(111) surface with MnO_2 is the most stable composition and will be further investigated in the remainder of this paper.

In the most stable MnO_2-modifed ceria structure, there is no terminal Mn=O manganyl species present. This presents an immediate difference with the VO_2-CeO_2(111) system previously studied. The corresponding structure for this composition with a terminal manganyl group lies 0.68 eV higher in energy than the structure shown in figure 2. Our most stable MnO_2-CeO_2 structure has a 3-coordinated Mn site with Mn-O distances of 1.79 Å to lattice oxygen and 1.70

Å to the two oxygen atoms in MnO_2. These oxygen atoms have Ce-O distances to surface Ce of 2.48 and 2.49 Å, while the lattice oxygen that binds to Mn has Ce-O distances of 2.32 Å and 2.66 Å; this oxygen is displaced by 0.43 Å from its lattice site to make the new bond to Mn, which lengthens one Ce-O bond involving this oxygen atom.

In the higher energy structure, with the manganyl group, the Mn-O distance to manganyl oxygen is 1.60 Å, similar to the vanadyl V=O distance in VO_2-CeO_2 and the titanyl distance (1.69 Å) in Ti=O bonds in TiO_2 nanoclusters [72] and the rutile TiO_2 (011)-(2x1) surface, with Ti=O distances of 1.62 Å [79]. The Mn-O distances involving oxygen coordinated to surface Ce are 1.72, 1.81 and 1.84 Å. These oxygen have Ce-O distances to surface Ce sites that are in the range of 2.27 – 2.42 Å.

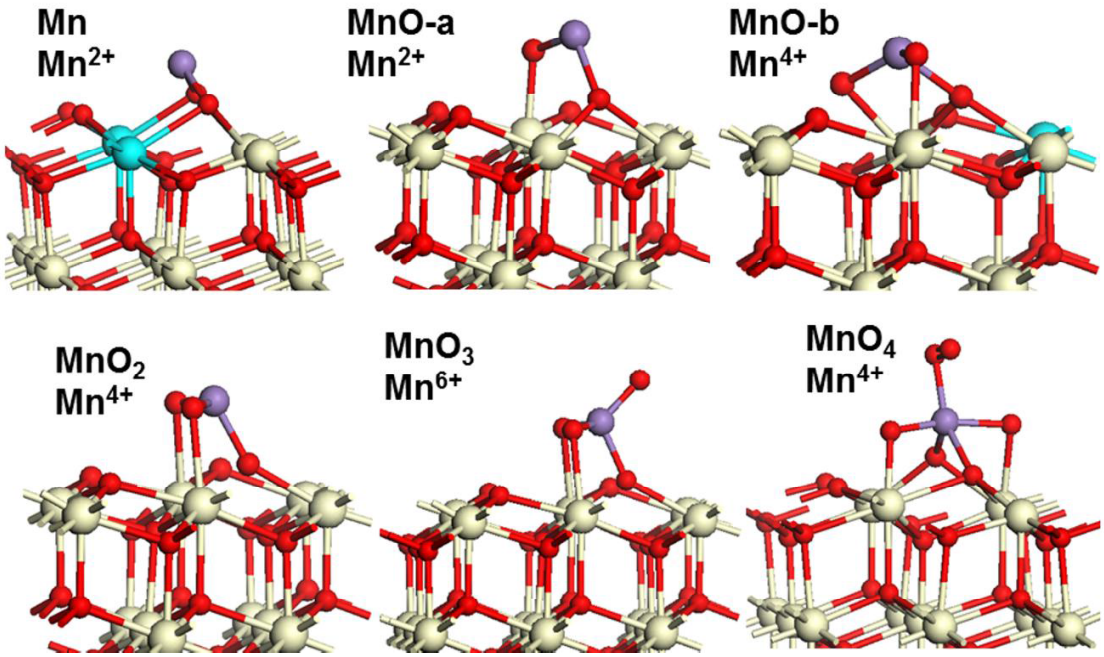


Figure 2: Relaxed atomic structures for MnO_n modified $CeO_2(111)$, n = 0, 1, 2, 3, 4 and the composition of each structure is indicated by the value of n in MnO_n. MnO-a and MnO-b refer to two different MnO-CeO_2 structures with the same composition that have the same energy (see text). Ce^{4+} is the white sphere, Ce^{3+} is the cyan sphere, O is the red sphere and Mn is the purple sphere. This colour scheme is used throughout the paper.

Figure 2 also shows the location of the reduced Ce^{3+} species (cyan coloured sphere) in MnO_2-$CeO_2(111)$; the supporting information shows the spin density isosurfaces for all the MnO_n-CeO_2 structures in Figure 2. Reduced Ce^{3+} species can be clearly seen from the spin density, with net Bader charges of +2.1 electrons (henceforth written as q=+2.1 e, which compares to net charges of +2.4 electrons (henceforth written as q=+2.4 e) for Ce^{4+} cations; see also refs [80, 81]. The spin density isosurface plots for Mn (and Cr) however, provide little useful information

regarding oxidation states. Therefore we have used Bader charges and spin magnetisations to assign oxidation states to Mn, Cr and Ce.

A neutral Mn species has a $4s^2 3d^5$ electronic configuration. In MnO_2-CeO_2, the Mn cation takes an Mn^{4+} oxidation state, which corresponds to an Mn $3d^3$ configuration determined from spin magnetisations; the corresponding net Bader charge is q=+1.84 e. This shows some differences to vanadium in VO_2-CeO_2(111) [25], where in the present case Mn does not take its highest oxidation state and does not involve ceria reduction.

We briefly discuss the salient features of the remaining MnO_n-CeO_2(111) compositions shown in figure 2. When Mn is adsorbed at the surface, we find, again differently to V-adsorption, that the structure whereby manganyl termination and a subsurface oxygen vacancy are present is 1.39 eV less stable compared to adsorption of Mn at the perfect surface. This most stable adsorption structure leads to formation of 2 Mn-O bonds, two reduced Ce^{3+} species in the surface, with q = +2.1 e, and an Mn oxidation state of Mn^{2+} ($3d^5$) with a net Bader charge of q=+1.2 e. The Mn-O distances to surface oxygen are 1.92 and 1.94 Å. This is different to the vanadium case, where V oxidises to V^{5+} forming five reduced Ce^{3+} species.

The MnO-CeO_2(111) structure is interesting because there are two different structures with the same energy (indicated by MnO-a and MnO-b in figure 2) and neither has a manganyl group, which is again in contrast to VO-CeO_2(111) in which a vanadyl group is present. In MnO-a-CeO_2(111), Mn is two-fold coordinated, with Mn-O distances of 1.84 Å (to oxygen in MnO) and 1.90 Å to surface oxygen. The latter oxygen atom has distances of 2.39 and 2.40 Å to surface Ce, which themselves have Ce-O distances in the surface typical of a Ce^{4+} species. The oxygen in MnO binds to a surface Ce site, with a distance of 2.17 Å . Mn is in the 2+ oxidation state, as

derived from a computed spin magnetisation of 5 3d electrons and a computed Bader charge of +1.3 e; the spin density shows that there are no reduced Ce^{3+} cations in the surface. While we can stabilize a structure for MnO-a-CeO_2(111) with reduced Ce^{3+} present, this lies 0.44 eV higher in energy than the most stable structure for MnO-a-CeO_2(111) that is shown in figure 2.

In the MnO-b-CeO_2(111) structure, which also has no manganyl group present, the spin density shows the presence of a Ce^{3+} cation, with a Bader charge of q=+2.1 e. In this structure, Mn takes an Mn^{4+} oxidation state, with a $3d^3$ electronic configuration and a Bader charge of q=+1.79 e. The Mn is 3-fold coordinated, with Mn-O distances of 1.78, 1.86 and 1.92 Å, while Ce-O distances involving oxygen shared by Mn and Ce are in the range of 2.26 – 2.45 Å. These oxygen species then have Ce-O distances ranging from 2.26 – 2.45 Å. The reduced Ce^{3+} cation has Ce-O distances between 2.42 and 2.53 Å, typical of Ce^{3+} cations.

We briefly present results for the MnO_3- and MnO_4-modified CeO_2(111) compositions. These are also quite different to VO_3- and VO_4-CeO_2(111). In MnO_3-CeO_2(111) a manganyl oxygen is present (with a Mn-O distance of 1.60 Å) and Mn binds to three further oxygen atoms, with Mn-O distances of 2×1.67, and 1.76 Å (the latter is to a surface oxygen atom). The spin density shows that there are no superoxide species or reduced Ce^{3+} cations present; all Ce cations have net Bader charges of +2.4 e. There is an apparent oxygen hole that is partially localised over 3 oxygen sites neighbouring the Mn. Finally, the spin magnetisation indicates an oxidation state of 6+ for Mn with a $3d^1$ configuration and a net Bader charge of +2.8 e.

In MnO_4-CeO_2(111), the spin density shows that there are no reduced Ce cations (q=+2.4 e) present. There is an apparent superoxide species present with an O-O distance of 1.30 Å, and are two further oxygen atoms with oxidation state O^-. The Mn cation has a $3d^3$ configuration, giving

an Mn^{4+} oxidation state and a net Bader charge of 2 electrons. Thus, the composition of MnO_4-CeO_2 can be written as $Mn^{4+}(O_2)^-(O^-)(O^-)$, i.e. there are two oxygen holes present which are spread over four oxygen atoms. Two of these oxygen atoms and one hole make up the superoxo species and the remaining oxygen hole is spread over the other two oxygen sites.

Comparing to VO_3- and VO_4-modified CeO_2(111) [25], the former also shows no superoxo or peroxo species and has a partially oxidized oxygen. In the latter, there is also a superoxo group present, but the two oxygen holes existing on MnO_4-CeO_2(111) are not present in this case.

An important point from this analysis is that while ceria always stabilizes the highest oxidation state of V in the VO_x modifier, i.e. 5+ , it can stabilize different Mn oxidation states, i.e. 2+, 4+, and 6+, that are not necessarily the highest possible, which is 7+. Furthermore, the oxidation state of Mn in MnO_x-CeO_2 depends on the composition. This difference arises from the stability of different oxidation states of Mn. In addition, the preference for Mn to reduce compared to Ce has been found in DFT studies of Mn-doped CeO_2(111), where Krcha et al. [13, 14] showed with a similar DFT+*U* set-up that upon oxygen vacancy formation in Mn-doped CeO_2(111), Mn preferentially reduces over Ce. This is therefore consistent with our findings that the preference is not necessarily for Mn to take the highest possible oxidation state and a range of oxidation states are therefore possible.

3.2. Modification with CrO_n Species

Figure 3 shows the stability plot for the different CrO_n species on the CeO_2(111) surface and figure 4 shows the final relaxed atomic structures for CeO_2(111) modified with CrO_n, where n = 1 – 4. At 1 atm pressure and at temperatures from 0 – 225 K, the CrO_4 species dominates and

from 225 – 775 K, that is in the range of temperatures that are important for catalytic reactions, the CrO_2 species is the most stable. Thus, we will focus our investigations on CrO_2-modified CeO_2(111).

In the most stable CrO_2-CeO_2(111) structure, a terminal Cr=O chromyl species is present, with a Cr-O distance of 1.60 Å, similar to the Mn=O and V=O distances. Chromyl terminations of oxidized Cr_2O_3 are known, e.g. [82 - 87]. The Cr-O distance to the other oxygen in CrO_2 is 1.69 Å and the remaining Cr-O distances are 1.85 Å. These oxygen atoms have Ce-O distances to surface Ce sites in the range of 2.32 – 2.50 Å.

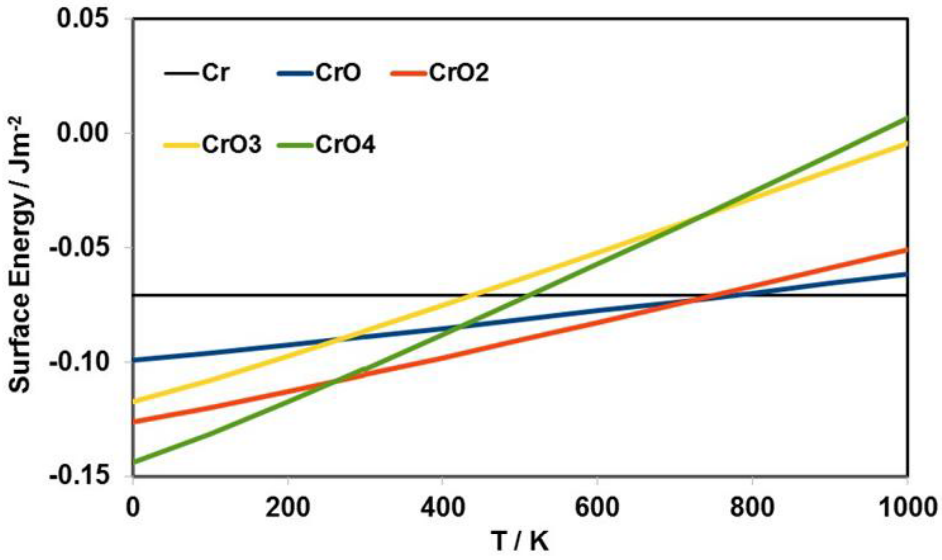


Figure 3: Plot of the surface energy of the CrO_n-CeO_2 system as a function of temperature at 1 atm.

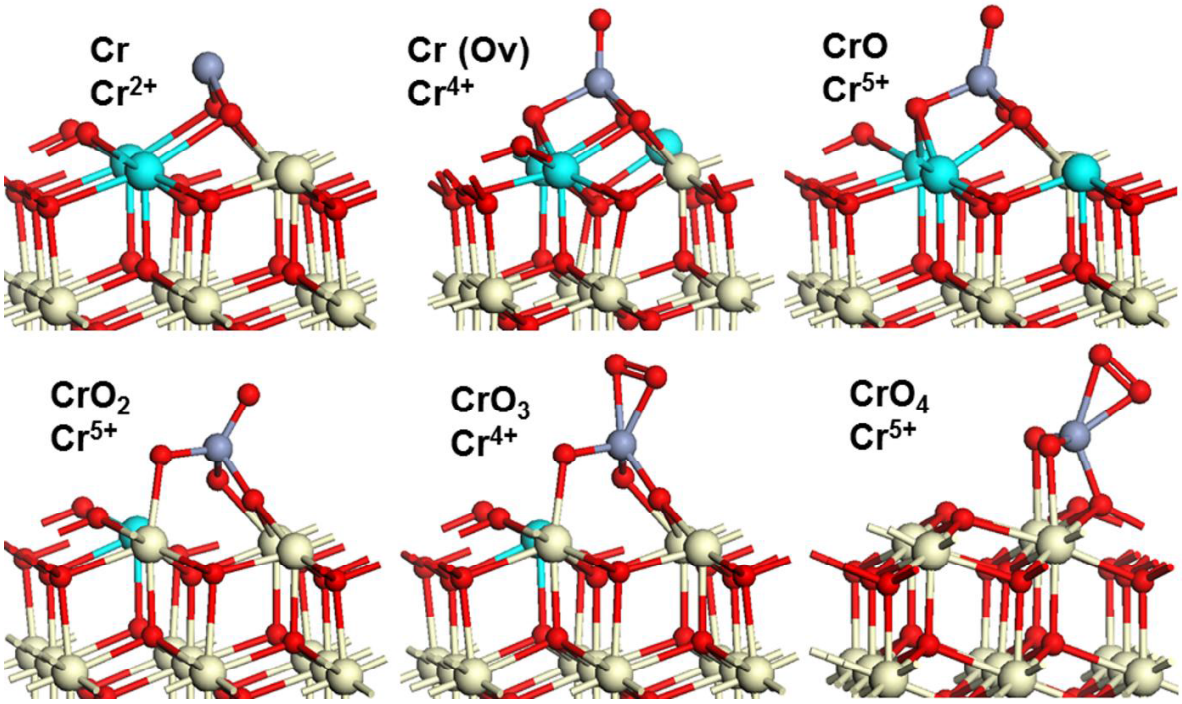


Figure 4: Relaxed structures for CrO_n modified $CeO_2(111)$. The structures are denoted by the value of n in CrO_n. Structures denoted Cr and Cr(Ov) are the same composition but in the latter a chromyl group is present with a sub-surface oxygen vacancy (see text for more details). Ce^{4+} is indicated by the grey spheres, Ce^{3+} by the cyan spheres, O by the red spheres and Cr by the blue spheres.

Figure 4 also shows the location of reduced Ce^{3+} species (see also figure S2 in the supporting information for spin densities) in CrO_2-$CeO_2(111)$. Similar to VO_2-modified $CeO_2(111)$ there is one reduced Ce^{3+} ion in the ceria surface and analysis of the local spin magnetisations indicates that the Cr 3d population is $3d^1$, indicating that a Cr^{5+} species is present in this structure, in a similar fashion to V; because a neutral Cr species has a $4s^1 3d^5$ electronic configuration, a Cr^{5+} species has a Cr $3d^1$ electronic configuration. The net Bader charges on Cr are +2.25 electrons

and +2.1 electrons on Ce^{3+}. Thus the ceria (111) surface is able to accept electrons and stabilize a high oxidation state of this transition metal species. This is not necessarily the highest possible oxidation state (although a Cr^{6+} is of course undesirable), similar to Mn. It is possible that the VO_x-CeO_2 system is able to accommodate both full V oxidation (with empty 4s/3d states) and a high degree of Ce reduction, irrespective of the composition. However, for Cr and Mn, there is more competition between ceria and Cr/Mn reduction so that it may not be possible to accommodate the highest oxidation states of these metals. The VO_x-CeO_2 species show a "special" vanadia-ceria synergy due to the V electronic configuration and its preference to oxidise [4, 25]. In any case, our results show that in terms of good activity for oxidation reactions, the VO_x-CeO_2 system is not unique, as discussed below.

We briefly discuss the salient features of the remaining CrO_x-CeO_2(111) structures. With adsorption of Cr at the surface, there are two possible structures. In the first structure, Cr adsorbs on the(111) surface in a similar fashion to Mn to form new Cr-O bonds to terminal oxygen atoms in the support and the spin density plots, spin magnetisation and net Bader charge of Ce ions indicate that Cr adsorption results in 2 Ce^{3+} ions (q=+2.1 e) in the surface. Cr then takes a 2+ oxidation state, with a Cr 3d population of 4 electrons and a net Bader charge of q=+1.28 e. The resulting Cr-O distances are 1.87 and 1.88 Å.

The more stable structure (by 0.51 eV) is that in which a chromyl Cr=O group is present together with a subsurface oxygen vacancy in the ceria support (denoted by the structure Cr(Ov) in figure 4). In this structure, the spin density, spin magnetisation and Bader charges show that there are three reduced Ce^{3+} species (q=+2.1 e). Cr has a Bader charge of +2.0 electrons, with the spin magnetisation showing a d^2 configuration and a Cr^{4+} oxidation state. The chromyl Cr-O distance is 1.62 Å and the Cr-O distances to remaining oxygen are 1.93, 1.95 and 1.96 Å.

The CrO-CeO_2(111) structure also has a chromyl group, with a Cr-O distance of 1.62 Å and the Cr-O distances involving O bound to surface Ce are 1.76, 1.82 and 1.83 Å. This is similar to the case of the VO modifier [4, 25]. In this composition, the spin density plot, spin magnetisation and net Bader charge also indicate the formation of three reduced Ce^{3+} ions (q=+2.1 e). For Cr in this structure, the net Bader charge is +2.24 electrons and the spin magnetisation indicates one 3 d electron, suggesting the formation of a Cr^{5+} oxidation state.

For CrO_3- and CrO_4-modified CeO_2 (111) superoxide species are present, with the spin density plot, spin magnetisation and net Bader charge showing the formation of a reduced Ce^{3+} species (q=+2.1 e) in CrO_3-CeO_2. This contrasts with VO_3-modified CeO_2(111), where there is a single oxygen hole present, but is similar to VO_4-CeO_2(111). In CrO_3-CeO_2, the O-O bond length in the superoxide is 1.36 Å and the Cr oxidation state is 4+, with a net Bader charge of +2.06 electrons and a spin magnetisation of 2; the overall composition is therefore Ce^{3+} Cr^{4+} (O_2^-) (O^{2-}). In CrO_4-CeO_2(111), the O-O bond length is 1.33 Å and the spin density indicates that no Ce^{3+} species are formed (the net Bader charge on all Ce cations is +2.4 electrons) and zero spin magnetisation. For Cr, the net Bader charge is +2.25 electrons and the occupation of the 3d states is $3d^1$, giving a Cr^{5+} oxidation state, with an overall composition of $Cr^{5+}(O^{2-})_2(O_2^-)$.

3.3. Probing Reactivity by O vacancy formation energy

The oxygen vacancy formation energy can be used as a descriptor of the activity of a catalyst in oxidation reactions that follow the Mars-van-Krevelen mechanism, including CO oxidation to CO_2 and the ODH of methanol to formaldehyde [4, 25, 26, 27]. In ODH reactions, after the oxidation cycle, a water molecule desorbs and an oxygen vacancy is formed in the catalyst.

Therefore, the oxygen vacancy formation energy relates to the reaction energy. Oxygen defect formation (completing the oxidative dehydrogenation) leaves two electrons, which can occupy either Mn/Cr 3d or Ce 4f states. Moreover, hydrogen abstraction by a surface oxygen species has been identified as the rate determining step [5, 88, 89]. For the particular case of methanol ODH the important H abstraction step is from a methoxy group that is bound to the catalyst. One of the electrons of the dissociated C–H bond forms a $CH_2O^{\bullet}$ surface radical, whereas the other is transferred with the adsorbed H which results in a reduced Ce site. If the reaction energy of the C-H bond dissociation step is relatively constant when considering different catalysts, the hydrogenation energies of the surface oxygen species can be used as an additional reactivity parameter [4, 27, 88]. This is because of the postulated linear relation between energy barriers and reaction energies (BEP principle). The interpretation of the reactivity parameters is simple. The more favourable the reduction of the catalyst is, i.e. the more exoenergetic the hydrogenation energy is (and the lower the defect formation energy), the higher the reactivity is. We therefore examine in this section the formation energy of oxygen vacancies in MnO_2-CeO_2(111) and CrO_2-CeO_2(111) and figure 5 shows the numbering of the oxygen vacancy sites that we have considered. We note that in MO_2-CeO_2(111), O13 and O14 belong to MnO_2 and CrO_2 and the remaining oxygen atoms belong to the CeO_2(111) surface. Table 1 gives the computed oxygen vacancy formation energy for each vacancy site upon removal of oxygen and ionic relaxation and the relaxed structures are shown in figure 6. The oxidation states of the transition metal and the number of Ce^{3+} species are also shown in table 1.

Before we proceed with the analysis of oxygen vacancy formation in MnO_2- and CrO_2-CeO_2(111), we present the computed oxygen vacancy formation energy for VO_2-CeO_2(111) using the present DFT+*U* set-up and models (in ref. [25] a different Ce PAW potential was

used). The VO_2 adspecies has a terminal V=O group and with its second O, which is the most labile oxygen in VO_2-CeO_2(111), it bridges to a Ce^{4+} surface ion. The corresponding oxygen vacancy has a formation energy of +0.82 eV, compared to +0.79 eV using the DFT+*U* set-up in [25] and +0.84 eV in a larger surface supercell [31].

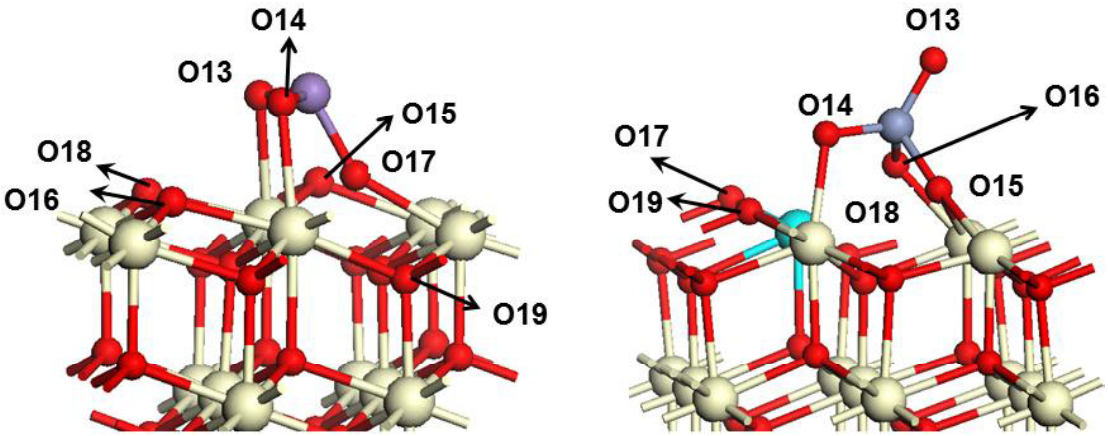


Figure 5: O vacancy site numbering in MnO_2-modified CeO_2 and CrO_2-modified CeO_2. See table 1 for the corresponding oxygen vacancy formation energies.

Table 1: Computed oxygen vacancy formation energies (E^{Ovac}), referenced to ½ O_2, for the oxygen vacancy sites in figure 5 for MnO_2-CeO_2 and CrO_2-CeO_2, in eV together with the Mn and Cr oxidation states and number of Ce^{3+} ions in the resulting MnO/CrO-CeO_2 systems.

MnO_2-CeO_2			
O vacancy site	**E^{Ovac} / eV**	**MnO-CeO_2**	
		Mn Oxidation State	**#Ce^{3+} species**
13	**1.03**	+2	0
14	**1.03**	+2	0
15	1.41	+4	2

16	**1.03**	+4	1
17	1.49	+2	0
18	**1.03**	+4	1
19	2.56	+4	2
CrO_2-CeO_2			
O vacancy site	**E^{Ovac} / eV**	**CrO-CeO_2**	
		Cr Oxidation State	**#Ce^{3+} species**
13	1.59	+3	1
14	1.87	+4	2
15	2.32	+5	3
16	1.46	+4	2
17	1.58	+4	2
18	**0.85**	+5	3
19	3.00	+4	2

From table 1, we see that the most stable vacancy site depends on the transition metal oxide modifier on CeO_2. For MnO_2-CeO_2 there are 4 stable oxygen vacancy sites; these divide into two groups: the first is on sites O13 and O14, which correspond to the structure denoted MnO-a in figure 2 and the corresponding relaxed atomic structures are shown in figure 6 (a) and (b). We see that these two structures are the same except for the orientation of the MnO adspecies. The second group is on sites O16 and O18 (figure 6 (c) and (d)), which correspond to the structure denoted MnO-b in figure 2 and here the surface oxygen removed is not neighbouring the Mn site. These two structures are the same except for the orientation of one bridging Mn-O bond. These oxygen vacancy sites have a formation energy of +1.03 eV which is a substantial reduction from the most stable oxygen vacancy site in the unmodified (111) surface, that is the subsurface oxygen with Ce^{3+} in nearest-neighbour cation sites which has an energy cost of 1.88 eV [36] and is not significantly larger than the oxygen vacancy formation energy computed for VO_2-CeO_2 (+0.82 eV). This suggests that MnO_2-CeO_2, would still be useful for the ODH of methanol.

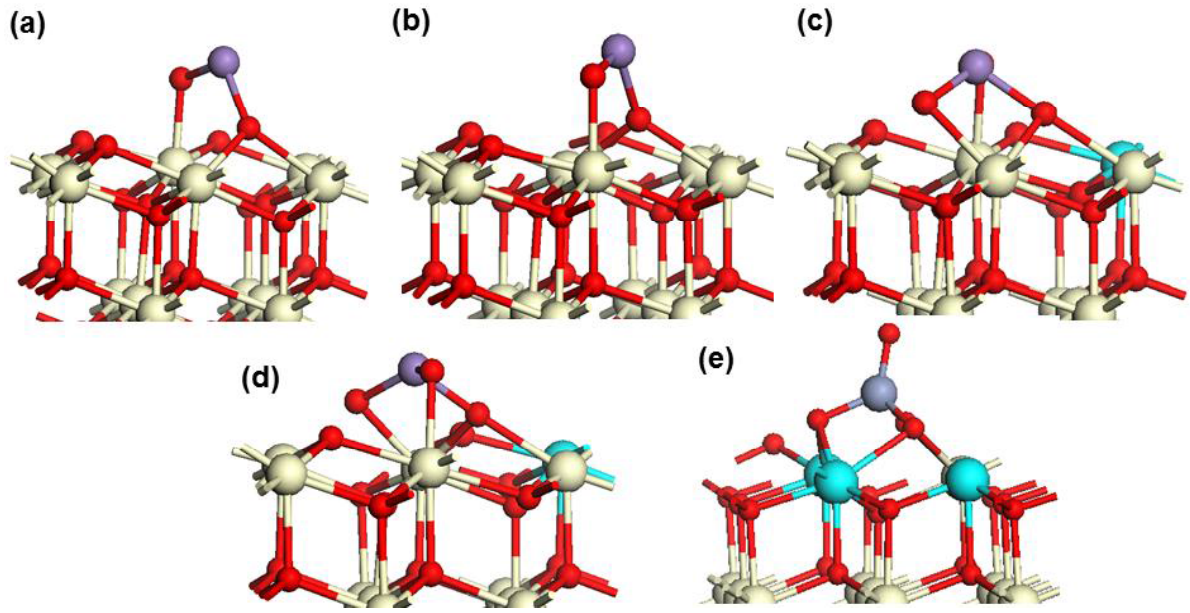


Figure 6: Atomic structure, for the most stable relaxed oxygen vacancy sites in (a), (b), (c) and (d) MnO_2-CeO_2 (see text) and (e) CrO_2-CeO_2. The colour coding is the same as figures 2 and 4.

The atomic structures of the stable oxygen vacancy sites in MnO-CeO_2(111) shown in figure 6(a) - (d) are already described in the discussion in Section 3.1. In the oxygen vacancy structures formed after removal of O13/O14, no reduced Ce^{3+} species are present in the MnO-CeO_2(111) system (the net Bader charge on Ce is q=+2.4 e and the spin magnetisation on all Ce is 0). The oxidation state of Mn is reduced from 4+ to 2+, with the spin magnetisation indicating a change in the Mn 3d occupation from $3d^3$ to $3d^5$ and a change in the net Bader charge from +1.9 to +1.36 electrons. For these oxygen vacancy sites, we cannot stabilize any MnO-CeO_2 structure with reduced Ce^{3+} species present indicating that Mn will be preferentially reduced upon creation of such vacancies. However for O16 and O18, the removal of surface oxygen does results in

reduction of one surface Ce atom to Ce^{3+}, with a net Bader charge of q=+2.1 e and a spin magnetisation of 0.98. Mn remains in a +4 oxidation state, with a net Bader charge of q=+1.79 e and a spin magnetisation that indicates a $3d^3$ configuration. In this structure (MnO-b), the lack of change in Mn oxidation state can arise from the reduction of one Ce cation and the fact that Mn now coordinates to 3 oxygen atoms rather than two as in the other MnO-a type structure. Thus upon reduction of the MnO_2-CeO_2(111) system there are two equally stable MnO-CeO_2(111) structures with different Mn and Ce reduction patterns, so that both possibilities are likely to be present in this modified CeO_2(111) system.

The most stable oxygen vacancy site in CrO_2-modified CeO_2(111) is O18, which is an oxygen originally in the ceria surface and the computed formation energy is +0.82 eV. The relaxed atomic structure of CrO-CeO_2 is shown in figure 6(e) and has been described in Section 3.2. In this structure, the chromyl Cr=O species is maintained and the Cr oxidation state does not change from +5: the net Bader charge on Cr is little changed at +2.24 electrons and the spin magnetisation is 0.98, indicating occupation of one 3d orbital. The two electrons left by the oxygen vacancy reduce two further surface Ce ions to Ce^{3+} (with net Bader charges of q=+2.1 e on each Ce^{3+} and a spin magnetisation of 0.95 electrons) to give 3 reduced Ce^{3+} sites, as shown in figure 6(e) and the supporting information. Thus, the CrO_2 modifier promotes the reduction of ceria, similar to VO_2-CeO_2(111).

We see a difference in the details of oxygen vacancy formation for the different transition metal oxide modifiers on ceria. Both VO_2-CeO_2 and CrO_2-CeO_2 lose an oxygen, with similar formation energies and atomic structures, to stabilize the +5 oxidation state in V and Cr which is coupled with reduction of ceria at a lower energy cost than the pure ceria surface. Thus, these modifiers enhance the reduction of the ceria surface and have a promoting effect on the reducibility of ceria

(111). This is important as it is known [5] that for VO_2-CeO_2, ceria is directly involved in the redox process in methanol ODH, as two electrons are accommodated in Ce f-states to form 2 Ce^{3+} cations, but V maintains the 5+ oxidation state. Actually, two different reaction pathways have been found that involve different sites of the supported catalyst system. In one path, OCH_3 species chemisorbs filling a pseudo surface oxygen vacancy and the H atom is transferred to an V−O−Ce interphase bond whereas in the other, a V–OCH_3 species forms and the H is transferred to the ceria surface, providing evidence for true cooperativity.

In contrast, MnO_2-CeO_2 is more complex. As discussed above, there are two types of oxygen vacancy sites that are equally stable – one vacancy type originates from the MnO_2 modifier and results in formation of a two-fold coordinated Mn^{2+} species with no reduced Ce^{3+} cations, which is the structure denoted as MnO-a in figure 2. The other vacancy type originates from the support and involves formation of Mn^{4+} and Ce^{3+} species, with one electron reducing Ce and the other electron is involved in the formation of a new Mn-O bond – this MnO-CeO_2 structure has three-fold coordinated Mn. As for VO_2-CeO_2, it is likely that different reaction pathways become operative at different temperatures that involve these labile oxygen atoms. In any case, modifications of CeO_2(111) with VOx, CrOx and MnOx show a reduction in the energy required to form an oxygen vacancy, irrespective of where the vacancy is created and this is the key point for the redox activity.

4. Adsorption of Hydrogen at MnO_2-CeO_2 and CrO_2-CeO_2

A further probe of the activity of modified ceria in ODH reactions is the adsorption of a hydrogen atom which will lead to changes in the oxidation states of the cations species, and the

rationale behind this was described in Section 3. We adsorb hydrogen at oxygen in each of the MnO_2- and CrO_2-CeO_2(111) systems and compute the adsorption energy with respect to half the total energy of a hydrogen molecule, focusing on the most stable H-adsorption site in each case, which is shown in figure 7 (see Supporting Information for other adsorption sites).

For MnO_2-CeO_2(111), the adsorption energy of hydrogen with reference to half the total energy of H_2 is -1.81 eV and for CrO_2-CeO_2(111) is -1.41 eV; for comparison, the adsorption energy of hydrogen on VO_2-CeO_2(111) is -1.45 eV, with both vanadyl [25] and non-vanadyl [4, 25, 31] adsorption sites showing similar stability. Again, we see the higher activity of MnO_2- and CrO_2-modified ceria compared to unmodified ceria (111), where the computed adsorption energy is -1.21 eV [4, 25] and -1.28 eV [90], strongly suggesting that these modifications to ceria would be beneficial to oxidation reactions.

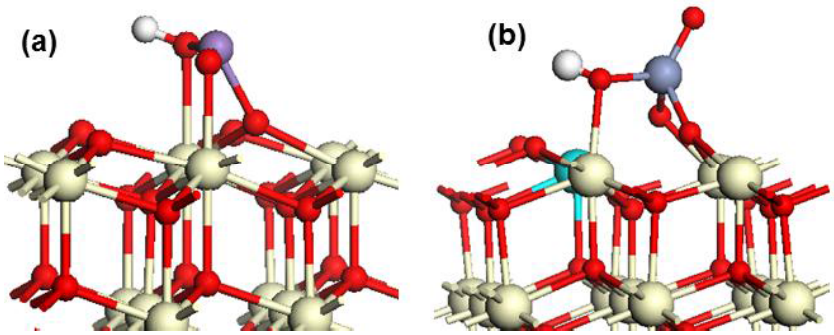


Figure 7: Atomic structure and Ce^{3+} sites for H adsorption at the (a) MnO_2-CeO_2(111) and (b) CrO_2-CeO_2(111) structures. The colour coding of figures 2 and 4 is used and H is the small white sphere.

Figure 7 shows the adsorption structure and the location of any reduced Ce^{3+} for hydrogen adsorbed at MnO_2-CeO_2(111) and CrO_2-CeO_2(111). When H adsorbs at VO_2-CeO_2(111), the adsorption is characterised by formation of a second Ce^{3+} species and the vanadium maintains its 5+ oxidation state [4, 25]. In contrast, when H adsorbs at oxygen in MnO_2-CeO_2, the most favourable adsorption site is at one of the oxygen atoms shared by Mn and the surface (O13 with reference to figure 5), i.e a Mn–O–Ce bond. After relaxation, an electron transfers from H to Mn, reducing Mn to a 3+ oxidation state with a net Bader charge of +1.90 electrons and a spin magnetisation of 0.95. There are no reduced Ce^{3+} species in the H:MnO_2-CeO_2(111) structure – all Ce have net Bader charges of +2.4 electrons, zero spin magnetisation and no occupied Ce 4f states. This shows that reduction of Mn can be favourable.

By contrast, when H adsorbs at an oxygen site that bridges Cr and Ce in the CrO_2-CeO_2 system, this is more stable than adsorption at the chromyl oxygen; the latter lies 0.13 eV higher in energy. The electron is transferred from H to Cr, reducing Cr from 5+ to 4+, with a net Bader charge of +2.06 electrons and preserving the single Ce^{3+} species and this is seen for all the H-adsorption sites we considered. This is different to the reduction process upon oxygen vacancy formation, in which Ce ions were reduced and Cr^{5+} was stabilized. Attempts to stabilize the H-adsorption structure in figure 7(b), in which the electron transfers to cerium, to give two reduced Ce^{3+} (with net Bader charges of +2.1 electrons on each Ce and a spin magnetisation of 0.95 electrons) in the support, gives a structure that lies 0.28 eV higher in energy.

5. Enhancing the Activity of VO_2-modified CeO_2 by doping of the ceria support

As mentioned in the introduction, doping of ceria is widely studied as an approach to modify the reactivity using oxygen vacancy formation as a descriptor. We, and others, have previously presented a number of studies showing that aliovalent dopants in ceria surfaces can lower the cost of oxygen vacancy formation over the undoped surface [8 – 15, 20]. A good example of this is Mg, with a 2+ oxidation state, which undergoes charge compensation of the lower valent Mg cation by forming an oxygen vacancy [9, 20]. The next oxygen vacancy that forms is the *active* oxygen vacancy and in the Mg-doped CeO_2(111) surface, the formation energy of this oxygen vacancy is reduced from 2.2 eV to 1.23 eV (within the same DFT+*U* set-up) [20].

In this section, we investigate if a model system composed of Mg-doped CeO_2(111) modified with VO_2 will show an increase in activity over VO_2 modified CeO_2(111) or Mg-doped CeO_2(111) and if the combination of ceria doping together with VO_2 modification can further promote the system reactivity. In figure 8 we show the atomic structure and the location of reduced Ce^{3+} in the VO_2-Mg:CeO_{2-x} structure, where CeO_{2-x} indicates that the charge compensating vacancy is present in the Mg-doped CeO_2(111) surface. In starting from VO_2-Mg:CeO_2, we find that similar to simple doping of the(111) surface [9, 20], a charge compensating oxygen vacancy forms in the Mg:CeO_2(111) support. In VO_2-Mg:CeO_{2-x}(111), one reduced Ce^{3+} ion is formed, with a net Bader charge of +2.1 electrons and a spin magnetisation of 0.95 electrons, while V and Mg have the fully oxidised V^{5+} (with zero spin magnetisation on V) and Mg^{2+} oxidation states.

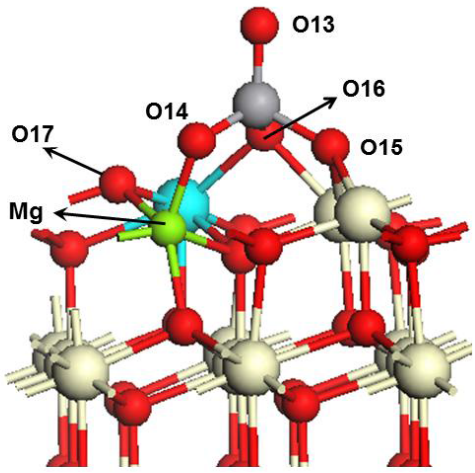


Figure 8: Relaxed atomic structure of Mg doped CeO_2(111) modified with VO_2 and a charge compensating oxygen vacancy in the ceria (111) surface, also showing the location of the oxygen vacancies examined in VO_2-Mg:CeO_{2-x}. The colour coding is grey spheres: Ce^{4+}, cyan spheres: Ce^{3+}, red spheres: O, grey sphere: V, light green sphere: Mg

In forming the active oxygen vacancy, we remove a number of oxygen atoms, shown in figure 8 and the computed oxygen vacancy formation energies are given in table 2. The most stable relaxed structure and distribution of Ce^{3+} species is shown in figure 9 for the example of the O14 vacancy site, with a formation energy of 0.60 eV, which is an oxygen removed from VO_2. The O16 and O17 vacancy sites have oxygen removed from the CeO_2(111) support with comparable formation energies of 0.60 eV. Thus, it appears that oxygen from both vanadia modifier and ceria can be removed as a result of the synergy between doping and surface modification of the CeO_2(111) surface. The formation of each of these oxygen vacancies produces two additional Ce^{3+} cations in the ceria (111) surface, which are characterised by net Bader charges of +2.1

electrons and occupation of a Ce 4f state on each Ce, while maintaining both the V^{5+} and Mg^{2+} oxidation states.

Compared to both Mg-doped CeO_2(111) [9, 20] and VO_2-CeO_2,(111) [4, 5, 25, 31], the combination of Mg doping and VO_2 modification appears to enhance the activity of ceria for oxidation reactions by reducing the oxygen vacancy formation energy. We can attribute this to the favourability of Ce reduction in VO_2-CeO_2 and the structural distortions induced by the smaller ionic radius Mg^{2+} dopant that allow a significant gain in energy upon relaxation, as discussed in earlier work [9, 20]. Figure 9 compares the oxygen vacancy formation process in VO_2-CeO_2(111), Mg:CeO_{2-x}(111) and VO_2-Mg:CeO_{2-x}(111) summarizing our findings. The promoting effect of VO_2 on ceria (111) remains but it is now further enhanced by cation doping of the surface.

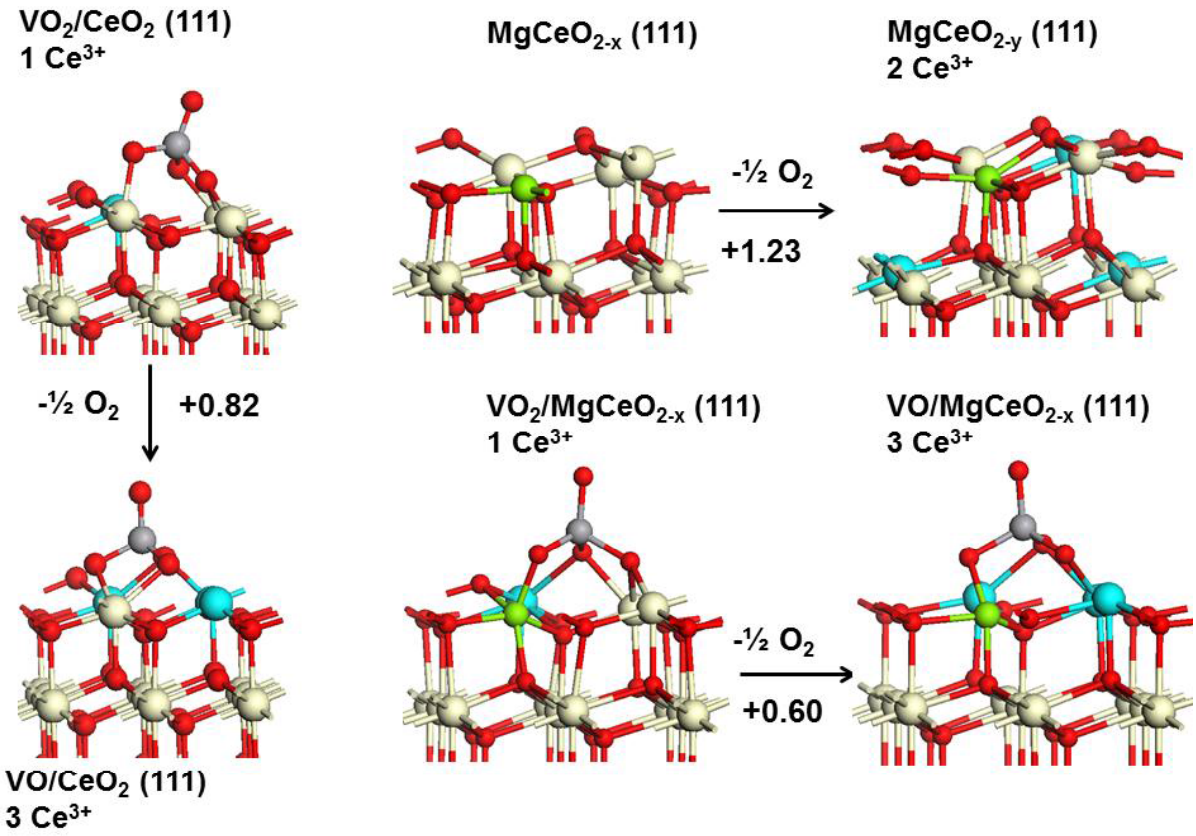


Figure 9: A summary of the oxygen vacancy formation process in VO_2-CeO_2(111), Mg-doped CeO_2(111) and VO_2-Mg:CeO_{2-x}(111). In each case we show the cost to form the most stable oxygen vacancy and the number of Ce^{3+} species present; in all structures, V and Mg take +5 and +2 oxidation states, respectively. VO_2-Mg:CeO_{2-x}(111) indicates the presence of an oxygen vacancy in the CeO_2(111) surface that compensates the Mg dopant oxidation state and the VO-Mg:CeO_{2-x}(111) structure shown corresponds to the removal of the oxygen atom labelled O14 (cf. fig.8). Colour coding is the same as earlier figures.

In examining the other oxygen vacancy sites, we find that when the vacancy forms at site O14, it removes an oxygen from the Mg-O-V linkage (i.e. from VO_2), but after relaxation, this oxygen is filled by O17 moving to repair the Mg-O-V linkage and maintain the VO_2. Thus, a vacancy at O14 and O17 lead to the same relaxed vacancy structure and therefore the oxygen vacancy is in the ceria (111) surface, so that the promoting effect of VO_2 remains but the overall reactivity is enhanced by coupling Mg doping with VO_2 modification of the surface.

Table 2: Computed oxygen vacancy formation energies (E^{Ovac}) for the oxygen vacancy sites in figure 9 for VO_2-Mg:CeO_{2-x}, in eV together with the V oxidation state and number of Ce^{3+} ions in the resulting VO-Mg:CeO_{2-x} system.

*This vacancy structure relaxes to the same structure as O14

O vacancy site	**E^{Ovac}**	VO-Mg:CeO_{2-x},	
		V Oxidation State	**Number of Ce^{3+}**
13	2.86	4+	2
14	**0.60**	5+	3
15	1.23	4+	2
16	**0.60**	5+	3
17*	**0.60**	5+	3

Finally, we consider the adsorption of hydrogen at the VO_2-Mg:CeO_{2-x} model structure. Figure 10 shows the final adsorption structure for H adsorbed at VO_2-Mg:CeO_{2-x}. The adsorption energy is -1.54 eV, which is similar to the VO_2-CeO_2(111) surface, with a computed adsorption energy of -1.45 eV [23] and we find the formation of a second reduced Ce^{3+} species in the surface, resulting from transfer of an electron from adsorbed hydrogen to the ceria (111) surface. Similar to VO_2 modified CeO_2, there is no change in the oxidation state of the V species.

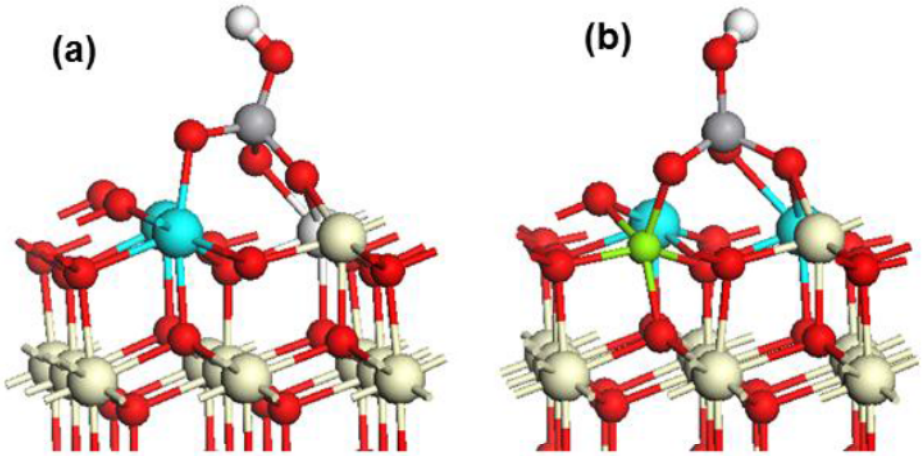


Figure 10: Relaxed atomic structure for hydrogen adsorbed at the (a) VO_2-CeO_2(111) and (b) VO_2-Mg:CeO_{2-x}(111) structures. Colour coding is the same as previous figures.

The oxygen defect formation energy undoubtedly indicate an enhanced activity of the VO_2/support system with a Mg doped support as compared to the undoped support. Also, it is enhanced compared to that of the Mg doped and bare ceria support themselves. The hydrogenation energies show less clear differences between the VO_2-CeO_2(111) and VO_2-Mg:CeO_{2-x}(111) systems, but both are predicted to be more reactive than the bare ceria support for which calculated H adsorption energies are -1.21 eV [4, 23] or -1.28 eV [66].

6. Conclusions.

The VO_x-CeO_2 system is a well known catalyst for oxidative dehydrogenation reactions, where vanadium oxide species are supported on ceria and a synergy between them drives the enhanced activity. Catalyst reduction in this system is driven by reduction of the ceria support. In this

paper, we have explored similar systems composed of MnO_x-CeO_2, CrO_x-CeO_2 and VO_2-Mg-CeO_2 (with an Mg doped ceria surface) to investigate if this enhanced activity is exclusive to VO_x-CeO_2. We use oxygen vacancy formation and hydrogen adsorption energies as descriptors for the oxidation activity of the new catalysts.

Combining total energy DFT+U calculations and thermodynamic concepts [25], we show that the most stable species in each case is MnO_2- and CrO_2-CeO_2, similar to VO_x-CeO_2. All modified ceria systems show more favourable energetics for oxygen vacancy formation and hydrogen adsorption compared to unmodified CeO_2, which indicates that VO_2-CeO_2 is not the only composite system of this type that can have an enhanced activity for oxidation reactions. Interestingly, we find that the mechanism behind the enhanced activity can be different in each case: CrO_2-CeO_2 and VO_2-Mg-CeO_2 show similar properties to VO_2-CeO_2 with ceria reduction upon oxygen removal stabilising the 5+ oxidation states of Cr and V. In contrast, in the MnO_2-CeO_2 system, Mn is preferentially reduced.

The results of this study on these new MO_x-CeO_2 systems shed further light on the factors involved in designing oxidation catalysts composed of metal oxides supported on ceria that should be taken into consideration in developing these catalysts. It would be interesting to see if these predictions will be verified experimentally.

Acknowledgements

MN acknowledges support from Science Foundation Ireland through the Starting Investigator Research Grant Program, project "EMOIN" grant number SFI 09/SIRG/I1620, the SFI-DEL-NSF US-Ireland program, project "SuSChem" grant number SFI 14/US/E2915 and the FP7 Project BIOGO, contract number 604296. MVGP acknowledges support from the Ministry of Economy and Competitiveness, project CTQ2012-32928. We also acknowledge computing resources provided by SFI to the Tyndall National Institute and by the SFI and Higher Education Authority Funded Irish Centre for High End Computing. Support from the European Commission for access to the JUROPA computer at FZ-Juelich through the FP7 Research Infrastructures Project PRACE-RI (contracts RI-261557, RI-283493 and RI-312763) is gratefully acknowledged. We acknowledge support from the European Union through the COST Action CM1104 "Reducible Oxide Chemistry, Structure and Functions".

References

1. I. E. Wachs, Catal. Today 2005, 100, 79

2. A. Dinse, B. Frank, C. Hess, D. Habel and R. Schomäcker, J. Mol. Catal. A: Chem. 2008, 289, 28

3. W. Daniell, A. Ponchel, S. Kuba, F. Anderle, T. Weingand, D. Gregory and H. Knözinger, Top. Catal. 2002, 20, 65

4. M. V. Ganduglia-Pirovano, C. Popa, J. Sauer, H. Abbott, A. Uhl, M. Baron, D. Stacchiola, O. Bondarchuk, S. Shaikhutdinov, and H. J. Freund, J. Am. Chem. Soc. 2010, 132, 2345

5. T. Kropp, J. Paier and J. Sauer, J. Am. Chem. Soc. 2014, 136, 14616

6. V. I. Anisimov, J. Zaanen, and O. K. Andersen, Phys. Rev. B, 1991, 44, 943.

7. S. L. Dudarev, G. A. Botton, S. Y. Savrasov, C. J. Humphreys, and A. P. Sutton Phys. Rev. B 1998, 57, 1505

8. E. W. McFarland and H. Metiu, Chem. Rev., 2013, 113, 4391

9. M. Nolan, J. Mat. Chem. 2011, 21, 9160

10. A. D. Mayernick and M. J. Janik, J. Phys. Chem. C 2008, 112, 14955

11 Z. Hu, B. Li, X. Y. Sun and H. Metiu, J. Phys. Chem. C 2011, 115, 3065

12 D. E. P. Vanpoucke, P. Bultinck, S. Cottenier, V. Van Speybroeck, and I. Van Driessche, J. Mat. Chem. A, 2014, 2, 13723

13. M. D. Krcha, and M. J. Janik, Langmuir, 2013, 29, 10120

14. M. D. Krcha, A. J. Meyernick and M. J. Janik, J. Catal., 2012, 293, 103

15. V. Shapovalov and H. Metiu, J. Catal. 2007, 245, 205

16. B. Li and H. Metiu, J. Phys. Chem. C 2010, 114, 12234

17. H. Y. Kim et al, J. Phys. Chem. C, 2008, 112, 12398

18. R. G. S. Pala and H. Metiu, J. Phys. Chem. C, 2007, 111, 8617

19. A. J. R. Hensley, et al. ACS Catal. 2014, 4, 3381

20. M. Nolan, Y. Lykhach, N. Tsud, T. Skála, Th. Staudt, K. C Prince, V. Matolín and J. Libuda, Phys. Chem. Chem. Phys., 2012, 14, 1293

21. P. Bera, K. R. Priolkar, P. R. Sarode, M. S. Hegde, S. Emura, R. Kumashiro and N. P. Lalla, Chem. Mater., 2002, 14, 3591

22. B. M. Reddy, L. Katta and G. Thrimurthulu, Chem. Mater., 2010, 22, 467

23. W. Tang, Z. Hu, M. Wang, G. D. Stucky, H. Metiu, and E. W. McFarland, J. Catal. 2010, 273, 125

24. V. J. Ferreira, P. Tavares, J. L. Figueiredo and J. L. Faria, Industrial & Engineering Chemistry Research, 2012, 51, 10535

25. C. Popa, M. V. Ganduglia-Pirovano and J. Sauer, J. Phys. Chem. C 2011, 115, 7399; 2012, 116, 18572 (Erratum).

26. H. Y. Kim, H. M. Lee, R. G. S. Pala, V. Shapovalov and H. Metiu, J. Phys. Chem. C 2008, 112, 12398

27. J. Sauer, and J. Döbler, Dalton Trans. 2004, 19, 3116

28. J. Sauer, In *Computational Modeling for Homogeneous and Enzymatic Catalysis*;Morokuma, K., Musaev, D. G., Eds.; Wiley-VCH: Weinheim, 2008; pp 231

29. T. Feng and J. Vohs, J. Catal. 2004, 221, 619

30. G. Deo and I. E. Wachs, J. Catal. 1994, 146, 323

31. C. Penschke, J. Paier and J. Sauer, J. Phys. Chem. C 2013, 117, 5274

32. J. Paier, T. Kropp, C. Penschke and J. Sauer, Faraday Discuss. 2013, 162, 233

33. G. Kresse, and J. Furthmüller, Comput. Mater. Sci. 1996, 6, 15

34. G. Kresse, and J. Hafner, Phys. Rev. B 1993, 47, 558

35. J. P. Perdew, K. Burke and M. Ernzerhof, Phys. Rev. Lett. 1996, 77, 3865

36. M. V. Ganduglia-Pirovano, J. L. F. Da Silva and J. Sauer, Phys. Rev. Lett. 2009, 102, 026101

37. S. Fabris, S. de Gironcoli, S. Baroni, G. Vicario, and G. Balducci, Phys. Rev. B 2005, 72, 237102

38. J. Paier, C. Penschke, and J. Sauer, Chem. Rev. 2013, 113, 3949

39. G. E. Murgida, and M. V. Ganduglia-Pirovano, Phys. Rev. Lett. 2013, 110, 246101

40. S. Fabris, G. Vicario, G. Balducci, S. de Gironcoli, and S. Baroni, J. Phys. Chem. B 2005, 109, 22860

41. M. Nolan, S. C. Parker and G. W. Watson, Surf. Sci., 2005, 595, 223

42. A. D. Mayernick and M. J. Janik, J. Phys. Chem. C 2008, 112, 14955

43. H.-Y. Li, H. F. Wang, X. Q. Gong, Y.-L. Guo, Y. Guo, G. Lu, and P. Hu, Phys. Rev. B 2009, 79, 193401

44. C. Zhang, A. Michaelides, D. A. King and S. J. Jenkins, Phys. Rev. B 2009, 79, 075433

45. J. C. Conesa, Cat. Today 2009, 143, 315

46. A. P. Amrute, C. Mondelli, M. Moser, G. Novell-Leruth, N. L´opez, D. Rosenthal, R. Farra, M. E. Schuster, D. Teschner, T. Schmidt, and J. J. P´erez-Ram´ırez, J. Catal. 2012, 286, 287

47. A. Peles, J. Mater. Sci. 2012, 47, 7542

48. J. J. Plata, A. M. Marquez and J. Fdez. Sanz, J. Phys. Chem. C 2013, 117, 25497

49. C. W. M. Castleton, J. Kullgren and K. Hermansson, J. Chem. Phys. 2007, 127, 244704

50. D. A. Andersson, S. I. Simak, B. Johansson, I. A. Abrikosov, and N. V. Skorodumova, Phys. Rev. B 2007, 75, 035109

51. M. Nolan, S. Grigoleit, D. C. Sayle, S. C. Parker and G. W. Watson, Surf. Sci. 2005, 576, 217

52. M. Nolan, Chem. Phys. Lett., 2010, 499, 126

53. M. Nolan, J. Phys. Chem. C, 2011, 115, 6671

54. M. Nolan, Chem. Phys. Lett., 2010, 492, 115

55. M. V. Ganduglia-Pirovano, A. Hofmann, and J. Sauer, Surf. Sci. Rep. 2007, 62, 219

56. M. Cococcioni and S. de Gironcoli, Phys. Rev. B 2005, 71, 035105

57. J. L. F. DaSilva, M. V. Ganduglia-Pirovano, J. Sauer, V. Bayer and G. Kresse, Phys. Rev. B 2007, 75, 045121

58. M. Huang and S. Fabris J. Phys. Chem. C, 2008, 112, 8643

59. M Nolan, in *Catalysis by Materials with Well-Defined Structures*, 2015, p. 159. Editors: Z. Wu and S. H. Overbury, Elsevier.

60. B. Meredig, A. Thompson, H. A. Hansen, C. Wolverton, and A. van de Walle, Phys. Rev. B 2010, 82, 195128

61. B. Dorado, M. Freyss, B. Amadon, M. Bertolus, G. Jomard, and P. Garcia, J. Phys.: Condens. Matter 2013, 25, 333201

62. J. P. Allen and G. W. Watson, Phys. Chem. Chem. Phys., 2014,16, 21016

63. M. T. Curnan and J. R. Kitchin, J. Phys. Chem. C 2014, 118, 28776

64. J. L. F. Da Silva, M. V. Ganduglia-Pirovano and J. Sauer, Phys. Rev. B 2007, 76, 125117

65. M Nolan, JS Mulley, RA Bennett, Phys. Chem. Chem. Phys. 2009, 11, 2156

66. H. J. Kulik and N. Marzari, in Fuel Cell Science: Theory, Fundamentals, and Biocatalysis, Edited by Andrzej Wieckowski and Jens K. Nørskov, 2010 John Wiley & Sons, Inc.

67. K. Palotas, A. Andriotis, A. Lappas, Phys. Rev. B 2010, 81, 075403

68. F. Zhou, M. Cococcioni, C. A. Marianetti, D. Morgan, and G. Ceder, arXiv: cond-mat/0406382

69. B. J. Morgan and G. W. Watson: Surf. Sci., 2007, 601, 5034

70. B. J. Morgan and G. W. Watson, J. Phys. Chem. C. 2010, 114, 2321,

71. M. Nolan, N. A. Deskins, K. C. Schwartzenberg, and K. A. Gray, J. Phys. Chem. C, 2016, 120, 1808

72. M. Nolan, A. Iwaszuk, K. A. Gray, J. Phys. Chem. C 2014, 118, 27890

73. L. Wang, T. Maxisch, and G. Ceder, Phys. Rev. B 2006, 73, 195107,

74. B. N. Cox, M. A. Coulthard and P. Lloyd, J. Phys F Metal Physics, 1974, 4, 807

75. G. Kresse and D. Joubert, Phys. Rev. B 1999, 59, 1758

76. JANAF Thermochemical Tables, 2nd ed.; Stull, D. R.; Prophet, H., Eds.; U.S. National Bureau of Standards: Washington D.C., 1971

77. A. Hofmann, and J. Sauer, J. Phys. Chem. B 2004, 108, 14652,

78. K. Reuter, and M. Scheffler, Phys. Rev. B 2001, 65, 035406

79. T. J. Beck, A. Klust, M. Batzill, U. Diebold, C. Di Valentin and A. Selloni, Phys. Rev. Lett., 2004, 93, 036104

80. A. Migani, K. M. Neyman, F. Illas, and S. T. Bromley, J. Chem. Phys., 2009, 131, 064701

81. H.-T. Chen and J.-G. Chang, J. Phys. Chem. C, 2011, 115, 14745

82. M. A. Henderson, K. Rosso, Surf. Sci., 2011, 605, 555

83. O. Bikondoa, W. Moritz, X. Torrelles, H. J. Kim, G. Thornton and R. Lindsay, Phys. Rev. B 2010, 81, 205439; Erratum Phys. Rev. B 2015, 91, 039910

84. M. Luebbe, and W. Moritz, J. Phys.: Condens. Matter 2009, 21, 134010

85. X.-G. Wang and J. Smith, Phys. Rev. B 2003, 68, 201402(R)

86. F. Rohr, M. Baeumer, H. J. Freund, J. A. Mejias, V. Staemmler, S. Mueller, L. Hammer, and K. Heinz, Surf. Sci. 1997, 372, L291–7; Erratum Surf. Sci. 389, 391

87. B. Dillmann, F. Rohr, O. Seiferth, G. Klivenyi, M. Bender, K. Homann, I. Yakovkin, D. Ehrlich, M. Bäumer, D. Ehrlich, H. Kuhlenbeck and H.-J. Freund, Faraday Disc. 1996, 105, 295

88. J. Döbler, M. Pritzsche, and J. Sauer, J. Am. Chem. Soc. 2005, 127, 10861

89. X. Rozanska, R. Fortrie, and J. Sauer, J. Phys. Chem. C 2007, 111, 6041

90. D. Fernandez-Torre, J. Carrasco, M. V. Ganduglia-Pirovano and R. Perez, J. Chem. Phys. 2014, 141, 014703